OPTICA

Space-time Fourier ptychography for *in vivo* quantitative phase imaging

MING SUN, KUNYI WANG, YOGESHWAR NATH MISHRA, SIMENG QIU, AND WOLFGANG HEIDRICH*

Visual Computing Center, King Abdullah University of Science and Technology (KAUST), Thuwal 23955-6900, Saudi Arabia
**wolfgang.heidrich@kaust.edu.sa*

Received 30 May 2024; revised 24 July 2024; accepted 9 August 2024; published 3 September 2024

Quantitative phase imaging of living biological specimens is challenging due to their continuous movement and complex behavior. Here, we introduce space-time Fourier ptychography (ST-FP), which combines a fast Fourier ptychography (FP) model based on compressive sensing with space-time motion priors for joint reconstruction of quantitative phase, intensity, and motion fields across consecutive frames. Using the same input data as compressive sensing FP, ST-FP increases the space-bandwidth-time product of the reconstructed complex image sequence while leveraging redundant temporal information to achieve robust reconstruction performance. The efficacy of this approach is demonstrated across various applications, particularly in observing living microorganisms undergoing rapid morphological changes and reconstructing amplitude and phase targets in motion. The improved phase retrieval capability of ST-FP enables digital refocusing, facilitating comprehensive three-dimensional analysis of microorganisms. This advancement paves the way for enhanced visualization of cellular processes, developmental biology studies, and investigations into life mechanics at the microscopic level.

https://doi.org/10.1364/OPTICA.531646

1. INTRODUCTION

Understanding dynamic structures and processes is essential for deciphering cellular function, revealing the mechanisms behind various morphological changes [1–4]. Representative super-resolution imaging, including structured illumination microscopy [5,6], confocal microscopy [7], two-photon microscopy [8], and other fluorescence-based techniques [9–16], are crucial for observing molecular information in dynamic studies. However, they encounter limitations including sample suitability, the need for well-controlled, customized optical setups, and risks of photobleaching and phototoxicity. In this context, quantitative phase imaging (QPI), a label-free method, emerges as a crucial tool for studying cells and microorganisms in their native states, free from chemical toxicity or photobleaching effects, and especially advantageous for analysis of live specimens [17–19].

QPI employs diverse methodologies to obtain phase information crucial for non-invasive studies of cellular dynamics, each with its advantages and limitations. Techniques such as interferometry require phase references, increasing system complexity and sensitivity to vibrations [20–22], whereas digital holography and wavefront sensing offer computational reconstruction and high temporal resolution but face challenges in resolution and sensitivity [19,23–25]. Phase retrieval differs from prior methods, using computational, non-interferometric methods, and reconstructing phase shifts from intensity image sequences under varied conditions. Following this path, one notable technique is defocused-based imaging via the transport of intensity equation (TIE) [26], which requires precise mechanical scanning or wavefront-separation components. Differential phase contrast (DPC) microscopy, another branch, acquires multiple images under varied half-plane illuminations to retrieve phase information, further expanding QPI utility in biological research [27,28]. Nevertheless, the practical application of QPI is constrained by the need for a microscope system capable of providing a large field-of-view (FOV) and subcellular resolution at video rate, which is challenging for capturing dynamic biological processes.

Fourier ptychography (FP) represents a significant advancement in QPI by simultaneously generating high-resolution (HR) images and quantitative phase from sequences of low-resolution (LR) images captured at varying illumination angles. This technique effectively solves the longstanding trade-off between resolution and FOV [29,30], paving the way for non-invasive cellular studies [31–35]. Notably, FP is lauded for its simplicity, cost-effectiveness, and accessibility [36]. Nevertheless, accurately observing the rapid activities of microorganisms remains a formidable challenge since traditional FP methods are hindered by their sequential data acquisition process. To mitigate this, recent advancements have introduced multi-camera systems to capture different band-limited images simultaneously, reducing the capture time [37]. Another approach is to use the single-shot method, employing diffractive gratings or configurations akin to light-field imaging setups, to capture the data in one snapshot, although they often involve compromises between the FOV and resolution

[38]. The advent of multiplexing illumination strategies marks a significant leap forward in high-speed FP [39,40]. FP multiplexing works have demonstrated the potential to reduce redundancy and shorten exposure times, enhancing the practicality of FP for dynamic studies. Our work builds upon these illumination strategies, introducing a novel time-domain optimization to achieve high-speed, high-resolution FP. Specifically, our computational method extends the space-bandwidth product (SBP) of the reconstructed complex image compared to the raw capabilities of the FP hardware. This innovation enables the documentation of microorganism dynamics with unprecedented detail, offering insights into complex biological phenomena such as the interlimb coordination of tardigrades and protozoan defense mechanisms against predation, thus enriching our comprehension of microbial ecology and survival tactics. [41–45].

Incorporating temporal information for moving object recovery has made significant strides in the computational imaging field [46–51]. Here we introduce space-time Fourier ptychography (ST-FP), which achieves dynamic FP reconstruction by integrating object reconstruction over time with parameterized motion tracking in an optimization framework, without requiring additional hardware. Expanding upon pioneering space-time reconstruction frameworks [52–54], our approach simultaneously reconstructs complex-value objects and dense velocity estimates from digital image correlation analysis of successive frames. We address this challenge using a novel splitting framework, as shown in Fig. 1. Initially, we utilize an enhanced FP imaging model under multiplexed illumination via compressive sensing [55] to mitigate fast imaging tasks. Object reconstruction is formulated as a compressive sensing problem with integrated smoothness and temporal consistency priors, and requires only a small number of iterations through the alternating direction method of multipliers (ADMM) [56]. Subsequently, we determine the optical flow between adjacent recovered frames using Huber-l_1 regularization [57]. By alternating between FP reconstruction and motion estimation [53], high-resolution QPI is achieved under rapid and freeform deformations of the object. See details in Section 2.B.

We explore various reconstruction scenarios utilizing our novel optimization method. Initially, we evaluate the performance of ST-FP in motion correction for various targets through both simulation and experiments. The results demonstrate a significant reduction in "blurring" artifacts while preserving resolution integrity. Subsequently, we showcase our technique for reconstructing living organisms with uncontrolled dynamics, particularly for tardigrades and rotifers. Our results exhibit high fidelity in capturing the details during their free movement. Leveraging the phase retrieval capability of FP, we achieve digital refocusing to visualize internal activity and structures of microorganisms. ST-FP has the potential to revolutionize our understanding of microbe locomotion and behavior and could inspire the development of microscale and soft-bodied robotics by drawing inspiration from the locomotion strategies of live microorganisms.

2. METHODS

A. Forward Model

The FP hardware typically consists of an LED matrix and a normal research microscope, as shown in Fig. 1(a). Each LED with index m results in a (spatially coherent) plane wave at the object $\mathbf{o}$, with the specific angle of illumination corresponding to the spatial frequency $\mathbf{k}_m = (k_{xm}, k_{ym})$. This process corresponds to a shift in the Fourier domain controlled by the angle of illumination, and then filtered by the pupil function $\mathbf{H}$ [29,30]. This resulting spectrum is then inverse Fourier transformed to form the intensity at the sensor plane:

$$\mathbf{I}_m(\mathbf{o}(\mathbf{r})) = \left|\mathcal{F}^{-1}[\mathcal{F}[\mathbf{o}(\mathbf{r})\exp(j\mathbf{k}_m\cdot\mathbf{r})]\mathbf{H}(\mathbf{k})]\right|^2, \quad (1)$$

where $\mathcal{F}$ and $\mathcal{F}^{-1}$ respectively represent the 2D Fourier transform and its inverse, and j is the imaginary unit. $\mathbf{r} = (x, y)$ and

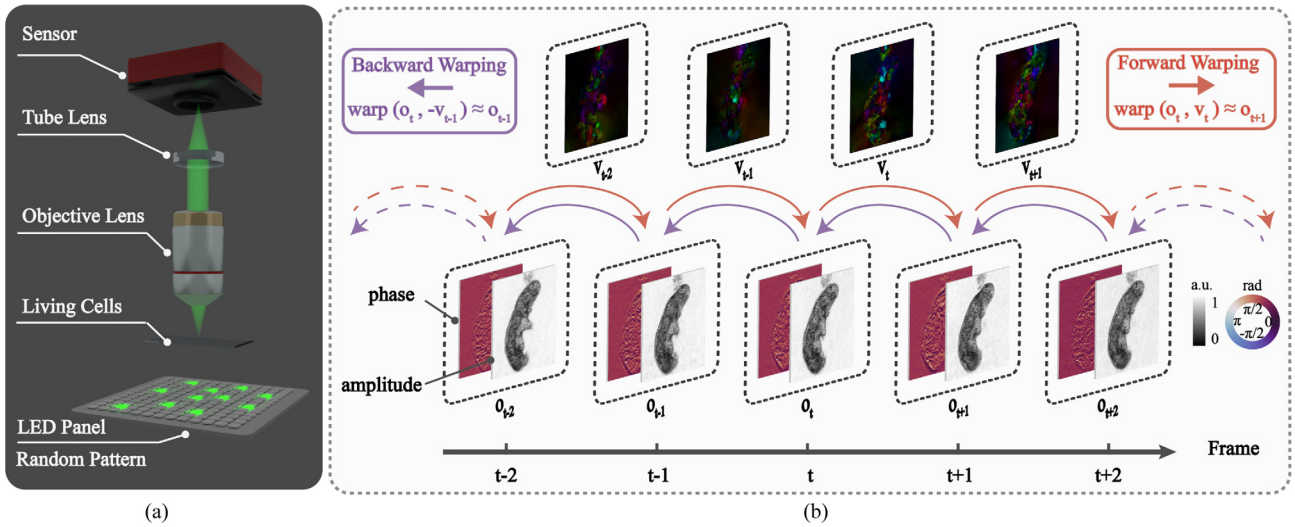

Fig. 1. Principle of space-time Fourier ptychography (ST-FP). (a) Schematic of ST-FP setup, including multiplexed LED illumination and the pathway through lenses to the sensor, captures the dynamics of living organisms. (b) To address rapid deformations between successive frames, a novel reconstruction approach utilizes warping to approximate intermediate frame states. For each timestamp, raw data $\mathbf{b}_t$ is captured under multiplexed illumination. Utilizing motion fields $-\mathbf{v}_{t-1}$ and $\mathbf{v}_t$, backward and forward warping are applied to estimate complex-valued objects $\mathbf{o}_{t-1}$ and $\mathbf{o}_{t+1}$, respectively. This approach effectively aggregates phase and amplitude information across time, resulting in increased reconstruction accuracy and resolution. This method aligns each captured raw frame with its temporal stamp, allowing for the reconstruction of objects even with significant motion, as opposed to the traditional scheme that requires negligible object movement.

$\mathbf{k} = (k_x, k_y)$ denote the coordinates at the spatial and frequency planes, respectively. For simplicity, we will use the notation $\mathbf{I}_m(\mathbf{o})$ in the following text, neglecting the explicit dependence on the spatial coordinate $\mathbf{r}$.

The traditional FP imaging procedure is to sequentially turn on each LED, which corresponds to extracting different areas of Fourier space. FP algorithms aim to stitch together these low-resolution (LR) sub-images in the Fourier domain to achieve a large effective NA, resulting in a high-resolution (HR) object reconstruction. At the same time the redundant information from the overlap regions allows for phase retrieval. However, long acquisition times limit the ability to image moving live samples using FP.

In our work we utilize and expand on multiplexed illumination [40,55,58] to mitigate this problem by simultaneously activating multiple LEDs according to a temporal sequence of different binary activation patterns $\mathbf{P}_t$. This yields a sequence of measured images corresponding to the activation image formation model:

$$\mathcal{A}_t(\mathbf{o}) = \sum_{m=1}^{N_{LED}} \mathbf{P}_{t,m}\mathbf{I}_m(\mathbf{o}), \tag{2}$$

i.e., the measurements are incoherent sums of the sub-images corresponding to the activated LEDs at each time. Using the theory of compressive sensing (CS), it is possible to reconstruct the complex object $\mathbf{o}$ from $N_{CS} < N_{LED}$ such measurements [55], therefore speeding up the imaging process.

While this CS approach simplifies the imaging of slow moving targets, it still assumes a *quasi-static* setting in which the object motion is negligible during the capture of the N_{CS} successive illumination patterns. For faster movements this assumption is violated even for short sequences, such as $N_{CS} = 2$, which is barely sufficient to achieve phase imaging or a super-resolution effect.

B. Space-Time Fourier Ptychography Framework

Here we introduce space-time Fourier ptychography (ST-FP), which aims to overcome the limitations of CS-FP and can reconstruct a *time-varying* object $\mathbf{o}_t$, which has a different, deformed geometry at every time t. The objective of ST-FP is to leverage temporal information to extract additional motion information from CS FP data, thereby increasing the space-bandwidth-time product of the reconstruction, and enabling imaging of dynamic states of the object across different frames. As a side benefit, ST-FP also provides an estimate of the object motion $\mathbf{v}_t$ over time.

This is achieved by solving an optimization problem that minimizes the least-squares error between the observed measurements and the predicted object states. For each frame t, the objective function is given by

$$\min_{\mathbf{o}_t} ||\mathcal{A}_t(\mathbf{o}_t) - \mathbf{b}_t||_2^2, \tag{3}$$

where $\mathcal{A}_t(\cdot)$ is the forward multiplexing function for frame t, $\mathbf{o}_t$ is the (complex-valued and *moving*) object at time t, and $\mathbf{b}_t$ represents the observed measurement. The ill-posed nature of this problem necessitates regularization to impose prior knowledge about the motion.

We impose a deformation prior by introducing motion fields between consecutive frames under the assumption that points on the specimen maintain the same intensity and amplitude under motion. This is a generalization of the *brightness constancy* assumption from the optical flow [59] and digital image correlation (DIC) [60] literature:

$$\mathbf{v}_t = \arg\min_{\mathbf{v}_t} ||\mathbf{D}_t|\mathbf{o}_t| + \mathbf{D}_s|\mathbf{o}_t| \cdot \mathbf{v}_t||_1, \tag{4}$$

where $\mathbf{D}_t$ and $\mathbf{D}_s$ represent the temporal and spatial discrete gradient operators, implemented as one-sided divided differences. $\mathbf{v}_t$ is the velocity (motion) field estimated for the motion from the amplitude image $|\mathbf{o}_t|$ to amplitude image $|\mathbf{o}_{t+1}|$. Here our intensity constancy assumption neglects minor defocusing effects. Note that this may not fully account for three-dimensional (3D) movements, particularly along the longitudinal (z-axis) direction. To address these potential deviations, we incorporate motion priors and temporal information to enhance robustness. Our method continuously tracks and updates motion fields, leveraging the redundant information across consecutive frames to correct for minor defocusing effects. Although $\mathbf{o}_t$ is a complex image in FP, we have found that utilizing only the amplitude for the motion estimation is more robust. For biological samples exhibiting a large degree of transparency, the bright field amplitude contrast may be too small to perform accurate tracking. However, since ST-FP uses multiplexed illumination patterns, each raw image also has a dark field illumination component, which enhances the intensity contrast even for transparent samples [29,30]. Thus, it is still possible to obtain useful intensity information even from pure phase-only samples (see Supplement 1 Fig. S4).

Given the estimated motion between two partial reconstructions, we can now *warp* or distort the reconstruction of the time t step to align with the reconstruction of the previous or next time step:

$$\mathbf{o}_{t+1} \approx \text{warp}(\mathbf{o}_t, \mathbf{v}_t) \quad \text{and} \quad \mathbf{o}_{t-1} \approx \text{warp}(\mathbf{o}_t, -\mathbf{v}_{t-1}). \tag{5}$$

Warping is defined as a pair of functions $\mathbf{o}_t$ and $\mathbf{v}_t$, which map a position in $\mathbf{o}_t$ to a position in another image $\mathbf{o}_{t+1}$ [61]. When the mapped point is not an integer, interpolation methods are used to estimate the value at non-integer coordinates. Here, we use the well-known bicubic interpolation method, resulting in a smooth surface using the values and derivatives of the surrounding integer samples [59,62].

Enforcing similarity between partial reconstructions achieved in this fashion is a powerful prior for improving overall reconstruction quality by aggregating information across time in a space-time framework. This is in contrast to classical CS-FP methods that assume a *quasi-static* object, where multiple successive lighting patterns can be imaged with negligible motion.

In the ST-FP framework, to address situations where the object undergoes fast deformations from frame to frame, we incorporate the warp-and-project method first introduced in x-ray tomography [53]. The principle behind this approach is depicted in Fig. 1(b).

Specifically, we exploit the inherent temporal coherence between contiguous frames to refine the joint estimation of object and motion. We formulate an optimization problem that concurrently considers neighboring frames, thereby enforcing consistency in the motion estimation process across the temporal dimension. By integrating this strategy, we effectively close the numerical reconstruction loop, ensuring that the reconstructed motion information closely aligns with the actual dynamics present within the scene. Overall, the joint optimization framework of ST-FP can be described as

$$\min_{\{\mathbf{o}_t,\mathbf{v}_t\}_t} \sum_{t=1}^{\mathrm{T}} \left\| \mathcal{A}_t(\mathbf{o}_t) - \mathbf{b}_t \right\|_2^2 + \alpha \sum_{t=1}^{\mathrm{T}-1} \|\mathbf{D}_t|\mathbf{o}_t| + \mathbf{D}_s|\mathbf{o}_t| \cdot \mathbf{v}_t\|_1$$
$$+\gamma \left(\sum_{t=1}^{\mathrm{T}-1} \left\| \mathcal{A}_{t+1}(\mathrm{warp}(\mathbf{o}_t, \mathbf{v}_t)) - \mathbf{b}_{t+1} \right\|_2^2 + \sum_{t=2}^{\mathrm{T}} \left\| \mathcal{A}_{t-1}(\mathrm{warp}(\mathbf{o}_t, -\mathbf{v}_{t-1})) - \mathbf{b}_{t-1} \right\|_2^2 \right)$$
$$+\beta \sum_{t=1}^{\mathrm{T}-1} \left(\left\| \mathbf{D}_s \mathbf{v}_{t,x} \right\|_{\mathrm{H}_{\mu_1}} + \left\| \mathbf{D}_s \mathbf{v}_{t,y} \right\|_{\mathrm{H}_{\mu_1}} \right) + \delta_1 \sum_{t=1}^{\mathrm{T}} \|\mathbf{D}_s \mathbf{o}_t\|_{\mathrm{H}_{\mu_2}} + \delta_2 \sum_{t=1}^{\mathrm{T}-1} \|\mathbf{D}_t \mathbf{o}_t\|_{\mathrm{H}_{\mu_3}}, \quad (6)$$

where the first term is the data fidelity term for the individual measurements. The second term is the optical flow term that jointly estimates the velocity/motion of the object. The next line incorporates the warp-and-project method, in which the partial reconstruction of the object at time t is *warped* forward (and backward) in time, and undergoes the image formation model $\mathcal{A}_{t+1}$ at that time (*project*), the result of which is compared to the measurement $\mathbf{b}_{t+1}$ obtained for that time. The final line has several smoothness regularizers for both the motion field (in space) as well as the object (in space and time). For these smoothness terms we utilize the Huber penalty function $||\cdot||_{\mathrm{H}}$, which provides a trade-off between the ℓ_1 and ℓ_2 norms. γ, α, β, δ_1, and δ_2 are weights of the different terms.

The joint optimization problem in Eq. (6) requires a special optimization strategy involving alternating between updating the complex images $\{\mathbf{o}_t\}_t$ and refining the motion estimates $\{\mathbf{v}_t\}_t$. We first initialize $\mathbf{o}_t$ in each time by $\mathcal{A}_t^{-1}(\mathbf{b}_t)$, where $\mathcal{A}_t^{-1}(\cdot)$ represents the pseudo inverse of $\mathcal{A}_t(\cdot)$ [55]. Then the $\{\mathbf{o}_t\}_t$ and $\{\mathbf{v}_t\}_t$ of two sub-problems are updated iteratively. The $\{\mathbf{o}_t\}_t$ update solver deals with object reconstruction by minimizing a complex objective function that balances FP data fidelity and regularization terms. It leverages the Huber loss function for robust optimization and updates complex variables by separating them into real and imaginary components. The $\{\mathbf{v}_t\}_t$ update solver, on the other hand, utilizes a multi-scale, coarse-to-fine strategy [59,62,63] to handle large displacements effectively, starting with a broader view and refining the estimation as it progresses to finer scales. Detailed procedures for the overall algorithm are provided in Supplement 1, S2.

3. RESULTS

A. Description of the Setup

For our experiments we utilize an FP setup following the diagram in Fig. 1(a). The commercial RGB LED matrix (Adafruit, 4 mm pitch) is placed at ∼75 mm away from the specimen plane. The central wavelength of the green channel is 525 nm, and the spectral linewidth is 20 nm. During the imaging process of each timestamp, multiple LED elements randomly selected are lit up at a time, which are driven with an Arduino controller board (ATmega 2560). The light transmitted through a transparent specimen was collected by a microscope objective (Mitutoyo, M Plan Apo 10×, 0.28 NA) and then directed to a camera via the tube lens (Thorlabs, TTL200-B) to form the image at the sensor. The camera (Triton, 5.4 MP Sony IMX490 CMOS, 3 μm pixel size) is synchronized with the LED matrix by the same controller via the coaxial cable that provides the trigger signal.

We experimentally set the system frame rate to be ∼24 Hz. Since we use a color sensor, color crosstalk exists from two effects [64]. First, the color LEDs used for illumination do not produce pure color light, but rather a broad spectrum centered on the nominal LED color. Second, the filtered pixel array of the image sensor similarly responds to a broad spectrum. Correcting for color crosstalk can be accomplished by generating a crosstalk map for the color separated [65], interpolated intensity maps. After the linear color unmixing process, we extract one color channel that we use to get the raw data captured with an exposure time of ∼36 ms.

B. Simulation Results

To evaluate the robustness and precision of dynamic objects, we present a comparative analysis of the conventional CS-FP technique and our proposed ST-FP method, as shown in Fig. 2. The analysis simulates four frames, each incorporating distinct motion patterns including translation along the y and x axes, and a composite of translation and rotation. This simulation is designed to emulate the behavior of both amplitude and phase parts of a complex optic field, thus providing a comprehensive evaluation of imaging capabilities. Our simulation employed a setup with a 10 × /0.28 NA objective lens, a sensor with a pixel size of 6 μm, a central illumination wavelength of 530 nm, and an LED array with a spacing of 4 mm. The LED array was situated 75 mm beneath the sample.

Figure 2 provides a comprehensive visualization of both amplitude and phase reconstructions, enabling an in-depth comparison. Figures 2(a) and 2(f) show the ground truth (GT) for amplitude and phase. Frames simulate distinct motion types: translations along the y axis, x axis, combined x-y axes, and a composite translation-rotation motion. Figure 2(b) illustrates the central LR sub-image obtained under the central illumination of the FP system. Figures 2(c) and 2(g) are the HR amplitude and phase reconstruction results from the standard FP method to serve as a baseline. The amplitude reconstructions for the CS-FP and ST-FP are presented in Figs. 2(d) and 2(e), respectively, where ST-FP maintains higher fidelity to the GT, especially under complex motion. Notably, the transition from the central LR image to our ST-FP method reveals marked improvements in resolution, evident in the clarity of line pairs within group 9 (left-up elements). Although the FP results show higher quality, they are computed for static frames and are provided for reference only. Please note that our method is designed for dynamic scenarios, where traditional FP cannot be applied. Therefore, in moving scenes, our method demonstrates the most suitable performance. Additionally, translations along the y axis using CS-FP enhance vertical detail contrast, though this inadvertently diminishes horizontal contrast. This effect is also observed with the x axis movement. Our ST-FP method, however, consistently maintains superior contrast and

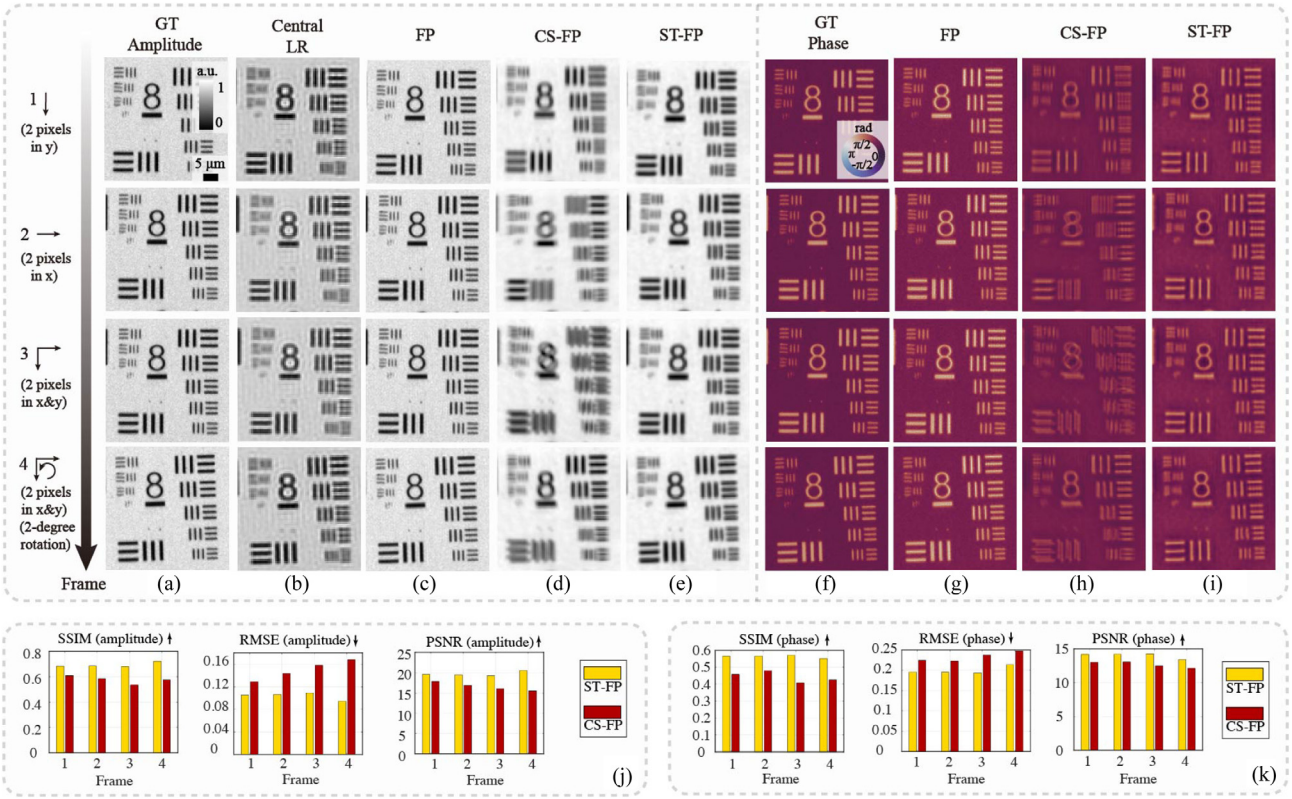

Fig. 2. Comparative analysis of dynamic simulation across four frames using a complex-valued USAF target. Frames simulate distinct motion types: translations along the y-axis, x-axis, combined x-y axes, and a composite translation-rotation motion. (a) Ground truth (GT) for amplitude. (b) LR sub-image under central FP system illumination. (c)–(e) Amplitude reconstruction for traditional FP method (144 sub-images used), CS-FP, and proposed ST-FP. (f) GT for phase. (g)–(i) Phase results of traditional FP, CS-FP, and our method. (j), (k) Comparison of amplitude and phase reconstruction quality against the GT, using SSIM, RMSE, and PSNR metrics for both CS-FP and ST-FP.

resolution in both directions, even in complex motion scenarios involving both translation and rotation. This is a significant departure from the previous motion-corrected FP [66], primarily addresses translational shifts. The phase reconstructions achieved using CS-FP and ST-FP are shown in Figs. 2(h) and 2(i).

The quantitative analysis, detailed in Fig. 2(j) for amplitude and Fig. 2(k) for phase, employs metrics such as SSIM, RMSE, and PSNR to quantify the enhancements provided by ST-FP over CS-FP. These metrics not only confirm the superiority of ST-FP in handling dynamic objects but also underscore its suitability for high-resolution dynamic imaging applications, where precise phase reconstruction is critical. For a more comprehensive set of data and in-depth analysis, the readers can refer to Supplement 1, S3.

C. Real Experiments with Controlled Motion

Here we test our method by moving static samples in the real world. First, red blood cells (RBCs) were imaged to assess the dynamic imaging capabilities of ST-FP. Initially, employing a conventional FP approach coupled with EPRY [67] for aberration correction, the static sample was imaged to establish a reference for quantitative phase reconstruction, utilizing 144 sub-images. Figure 3(a) presents the full FOV original LR image captured under a singular centered LED and the region of interest (ROI). Figures 3(b) and 3(c) are the HR amplitude and phase reconstruction results from the standard FP method. They serve as a baseline for comparing the performance of our method against conventional techniques. Subsequently, we induced sample motion by manually translating the stage along one axis to simulate dynamic conditions. We leveraged a fast Fourier transform (FFT)-based image registration algorithm [68] to estimate the global shift, initializing the optical flow computations. Figure 3(d) illustrates the raw data captured. Figures 3(e) and 3(f) depict the amplitude results at different timestamps using the CS-FP method and ours, respectively. Similarly, Figs. 3(g) and 3(h) display the corresponding phase results. The amplitude and phase outcomes by CS-FP show a marked degradation in clarity and contrast over time due to sample movement. ST-FP maintains a consistent quality across all frames. The speed of movement was estimated in pixels per frame (PPF). In Fig. 3, the speeds for each frame were about 0.83, 2.17, 3.52, 4.04, 5.59, and 7.14 PPF, calculated by averaging the flow values of each frame. The variances in speed for each frame were about 0.01, 0.01, 0.04, 0.02, 0.04, and 0.01 PPF. These speeds were chosen to represent a range of movement conditions. The robustness of ST-FP is particularly evident in the phase images, where CS-FP exhibits significant blurring and distortion of the phase profiles, while ours presents a clear and stable reconstruction of the phase information throughout the sequence (see Visualization 1). The ability to preserve the quality of both amplitude and phase information over time is indicative of the potential of ST-FP for real-time biomedical imaging applications, where motion is an intrinsic challenge.

We further demonstrate the digital refocusing capability of ST-FP, leveraging in-iteration phase retrieval to compensate for defocusing [69,70]. The results show notable improvements in

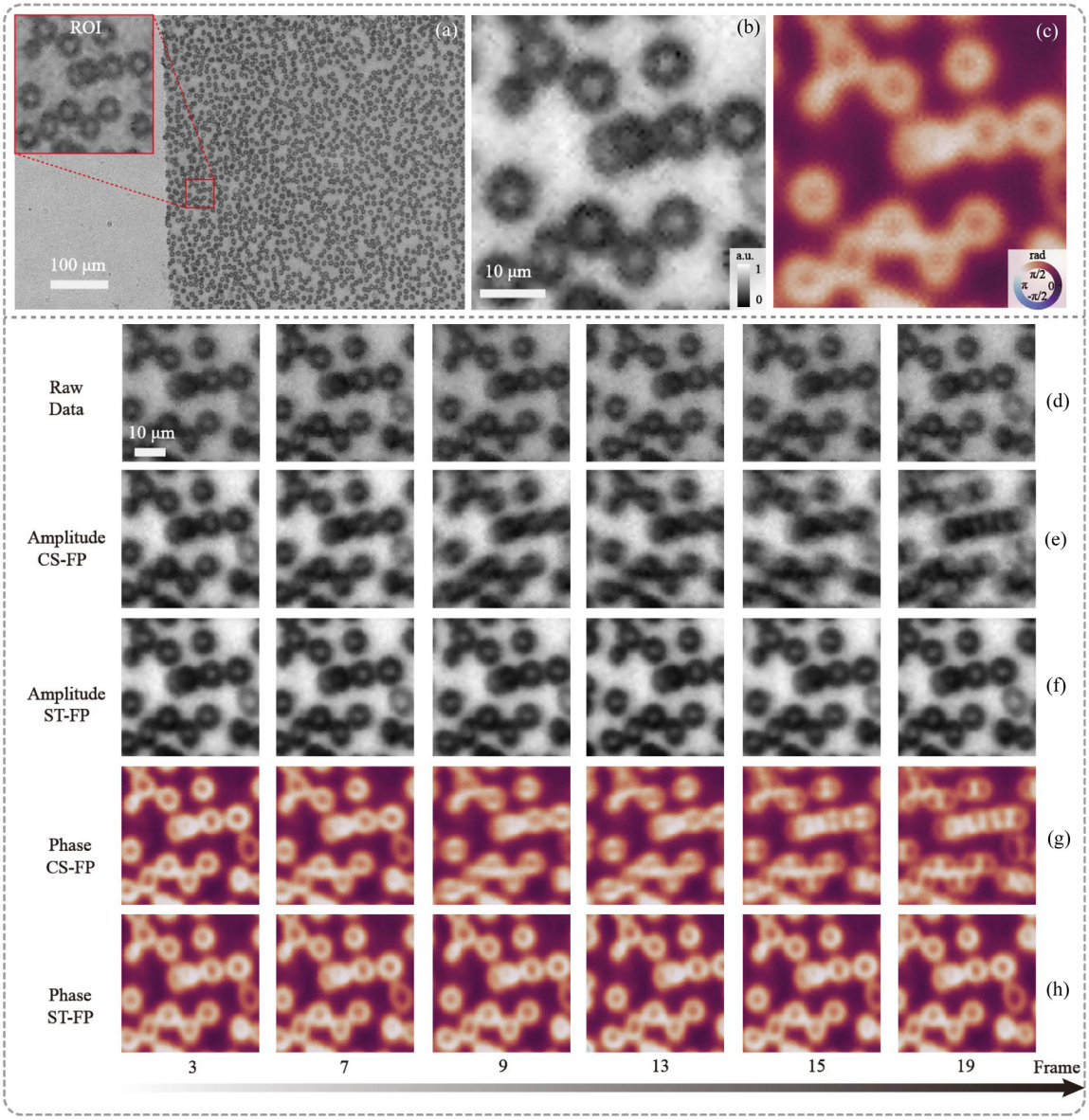

Fig. 3. Dynamic ST-FP imaging of red blood cells (RBCs). (a) Full FOV LR image captured under central LED illumination. (b), (c) Show the HR reconstructed amplitude and phase results, respectively, obtained from the standard FP algorithm when the sample is static, providing baseline reference. (d) LR raw data. (e), (g) Illustrate the amplitude and phase results, respectively, over time using the conventional CS-FP method, highlighting the susceptibility to motion-induced degradation. (f), (h) Present the temporal amplitude and phase results by ST-FP, demonstrating enhanced stability and image quality under dynamic conditions. The movement speeds in the raw data were estimated as 0.83, 2.17, 3.52, 4.04, 5.59, and 7.14 PPF. The variances in speed for each frame were about 0.01, 0.01, 0.04, 0.02, 0.04, and 0.01 PPF, respectively.

edge clarity and sharpness at various defocusing distances, validating the ability of ST-FP to dynamically achieve precise focus (see Visualization 2 and Supplement 1, S4).

The resolution capability of the ST-FP method was further substantiated by a pure amplitude USAF resolution target. A conventional FP technique was employed to capture LR images of the static target from 144 sub-images. Figures 4(a) and 4(b) display the full FOV and the ROI, respectively. The HR reconstruction obtained through the standard FP method is shown in Fig. 4(c), establishing a reference for comparison. To introduce dynamic imaging conditions, manual translation of the target along one axis was performed using a translation stage. Similarly, an FFT-based technique quantified the shift [68], providing an initial parameter for optical flow computations. Under dynamic conditions, the conventional CS-FP method experienced difficulties, with a noticeable decline in image sharpness and contrast as illustrated in Fig. 4(d). By contrast, our method demonstrated significant enhancements in image quality preservation amid motion, as shown in Fig. 4(e). The performance is also quantitatively supported by line plots derived from elements in group 9. Movement speeds were estimated as 0.53, 0.29, 1.06, 2.80, and 3.98 PPF. The corresponding variances in speed were 0.04, 0.03, 0.07, 0.18, and 0.04 PPF, respectively. While line plots from the CS-FP method exhibit pronounced fluctuations indicative of vulnerability to motion-induced effects, line plots from ST-FP display markedly less variability. ST-FP achieved a 20% improvement in full-pitch resolution along one axis, reaching 1.560 μm compared to 1.875 μm under single-LED illumination. This results in a

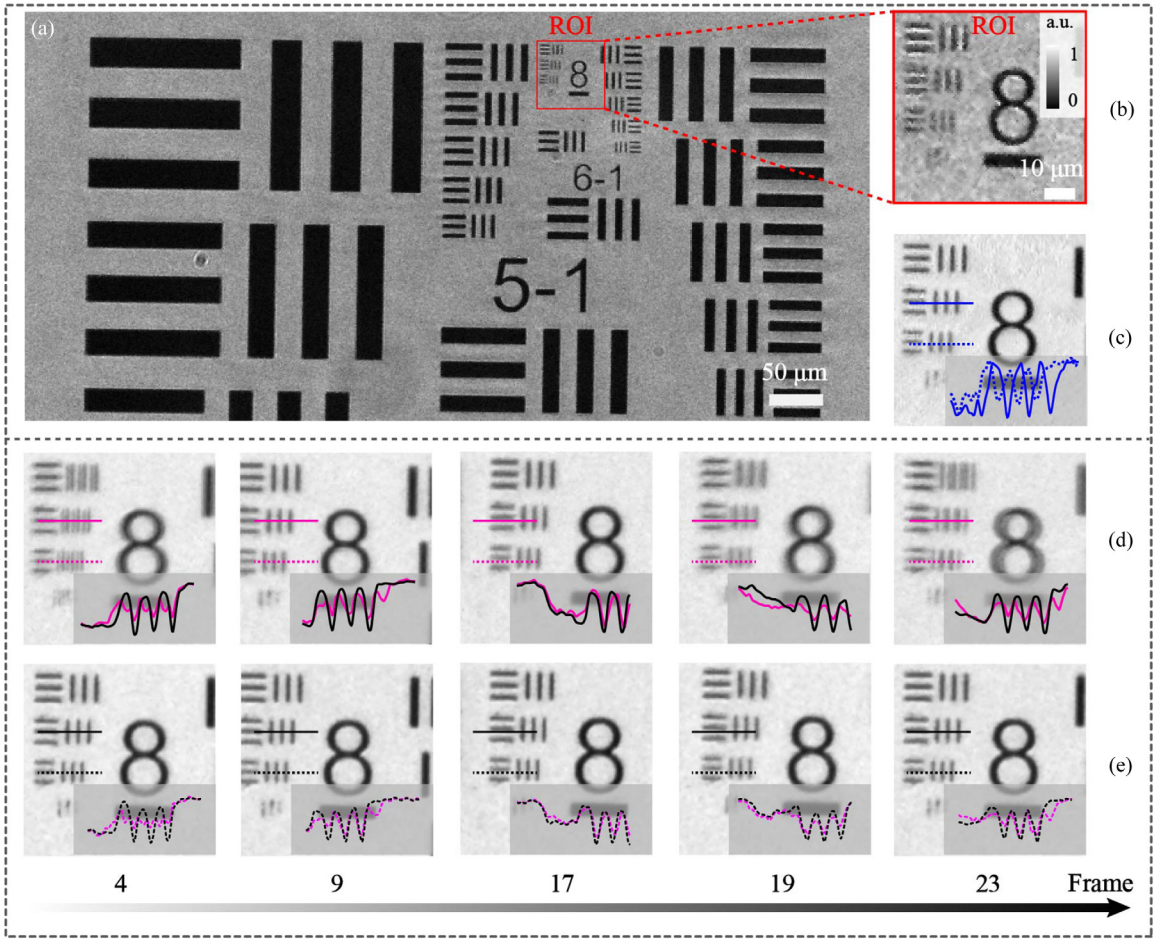

Fig. 4. Comparative analysis using moved pure amplitude USAF target. (a) Full FOV LR image of the target captured with a single LED. (b) Zoomed ROI. (c) HR reconstruction of the target using the standard FP method. (d) The sequence of results under dynamic conditions by CS-FP. The line plots show the susceptibility to motion. (e) The sequence of images by ST-FP illustrates robust amplitude estimation with reduced variability in line plots. Movement speeds were 0.53, 0.29, 1.06, 2.80, and 3.98 PPF. The corresponding variances in speed were 0.04, 0.03, 0.07, 0.18, and 0.04 PPF, respectively.

$1.2 \times 1.2 = 1.44$ times increase in the 2D case for SBP. Together with the recovered phase, ST-FP therefore increases the space-bandwidth-time product (SBP-T) from the raw image stream by a factor of 2.88.

Compared to CS-FP, ST-FP produces a substantially higher output frame rate at the same time as a higher spatial resolution. In CS-FP, an important parameter is the number of illumination patterns N_{CS} from which to reconstruct a complex image. For static targets, the achieved spatial resolution increases with N_{CS}. However, for dynamic targets, motion artifacts increase with N_{CS}, limiting the spatial resolution. At the same time, the output frame rate is also reduced by a factor of N_{CS}. Figures 4(d) and S4(d) in Supplement 1, S4 show that even for $N_{CS} = 2$ the spatial resolution is already compromised along the (horizontal) motion direction, with a super-resolution effect being achieved only in the orthogonal (vertical) direction. Supplement 1, S6 shows that and increasing the number of patterns further exacerbates the problem.

The resolution of CS-FP for dynamic targets was calculated by selecting a relatively motionless frame, representing the optimal performance that CS-FP can achieve under motion conditions. CS-FP achieves a resolution of 1.96 μm (group 9, line pair 1, as seen in the ninth frame of Fig. 4(d) and the fourth frame of Fig. S4(d)), while ST-FP achieves a resolution of 1.56 μm [group 9, line pair 3, as seen in Figs. 4(e) and S4(e)]. This results in a resolution improvement factor of 1.26×. When combined with a temporal resolution improvement by a factor of two compared to CS-FP, the SBP-T of ST-FP is $1.26 \times 1.26 \times 2 = 3.18$ times higher than that of CS-FP, reaching 1.82 megapixels per second. This performance was achieved over a 0.40 mm^2 FOV, capturing 0.16 megapixels within 90 ms. We note that higher-frame-rate cameras and illumination hardware could increase the SBP-T of all methods, with ST-FP being able to deal with faster motion than the competing methods. More detailed analysis and comparisons can be found in Visualization 3, Visualization 4, and Supplement 1, S4.

The data processing for our algorithm was performed on a CPU (AMD EPYC 7763 64-Core Processor) using MATLAB R2022b. The computational complexity of our algorithm is challenging to express in closed form due to the interplay of various components and it primarily involves two parts: optical flow estimation and ADMM iterations. In general, for sequences consisting of 24 frames with each raw image having a resolution of 250 × 250 pixels, the total running time for processing was approximately 56 min after two iterations.

D. Experiments with Uncontrolled Motion – Live Microorganisms

Figure 5 presents a comparative analysis between CS-FT and ST-FP in the reconstruction of a live rotifer. Figures 5(a) and 5(b) illustrate the raw data captured and a zoomed-in region for detailed examination, respectively. CS-FT employs data from multiple time frames to reconstruct a single frame, assuming minimal object movement during intermediate frame times. While this method benefits from the aggregation of information, aiding in HR image reconstruction, any movement in the intermediate period can violate the quasi-static assumption, leading to significant artifacts, as shown in Figs. 5(c) and 5(e). It is noteworthy that CS-FP can produce inaccurate details due to its time-mixed recovery approach, challenging its reliability. In contrast, ST-FP utilizes single-frame time images for reconstruction. Although this approach is inherently ill-posed and yields only marginal HR improvement, the spatial and temporal regularization in the optimization process demonstrates satisfactory performance [see Figs. 5(d) and 5(f)]. In comparison to CS-FP, our method shows significant improvements, particularly in phase reconstruction quality and resolution, which is crucial for accurate QPI in dynamic scenarios. It notably achieves sharp amplitude details and a saturated phase with minimal background noise (see Visualization 5).

We also demonstrate the digital refocusing capability of our proposed method. In Fig. 6, the optical field of a previously analyzed rotifer is digitally propagated through various defocusing distances (see Visualization 6 for more details). Each row corresponds to a specific frame time, illustrating the effectiveness of digital refocusing in achieving the correct focus plane across different areas and in sharpening the edges of originally blurry regions, as indicated by the red arrows.

We then contrast the reconstruction outcomes under three different scenarios to demonstrate the impact of various priors. The first case relies solely on the data fidelity term, which is marred by noise and a lack of recovery of high-frequency information due to insufficient priors. The second one is incorporating smoothness priors for space and time. The third one (ST-FP) considers dynamic uniformity between successive frames and reveals more distinct details of the inner structure and boundaries. Detailed results and analysis are provided in Supplement 1, S5.

To prove the versatility of our method, we demonstrate it on various samples, including a faster live rotifer (see Visualization 7 and Visualization 8) and another tardigrade with more complex movement (see Visualization 9 and Visualization 10). Please refer to Supplement 1, S5 for more details.

4. DISCUSSION AND CONCLUSIONS

In terms of future enhancement, ST-FP has the potential for the 3D reconstruction of dynamic processes, particularly when used in conjunction with tomography techniques [71]. In fact, significant and rapid movements on the z-axis could affect the accuracy of the optical flow, leading to potential deviations in the quality of the reconstruction of our method. Future work will focus on integrating depth information and improving our model to explicitly handle 3D movements more explicitly. As sensor frame rates continue to advance, ST-FP can be applied to capture faster movements, such as those of paramecium [46] or C. elegans [72,73]. Also, the non-linear imaging processes and inverse solutions inherent in multiplexed FP models could be resolved with the aid of deep learning techniques [49,74,75], thereby expediting and enhancing recovery accuracy.

Our algorithm has the flexibility to allow it to be integrated with different types of imaging hardware, enhancing the ability to capture high-resolution, dynamic processes. However, the limitation of our algorithm is its inability to accommodate significant displacement within a single captured frame. In particular,

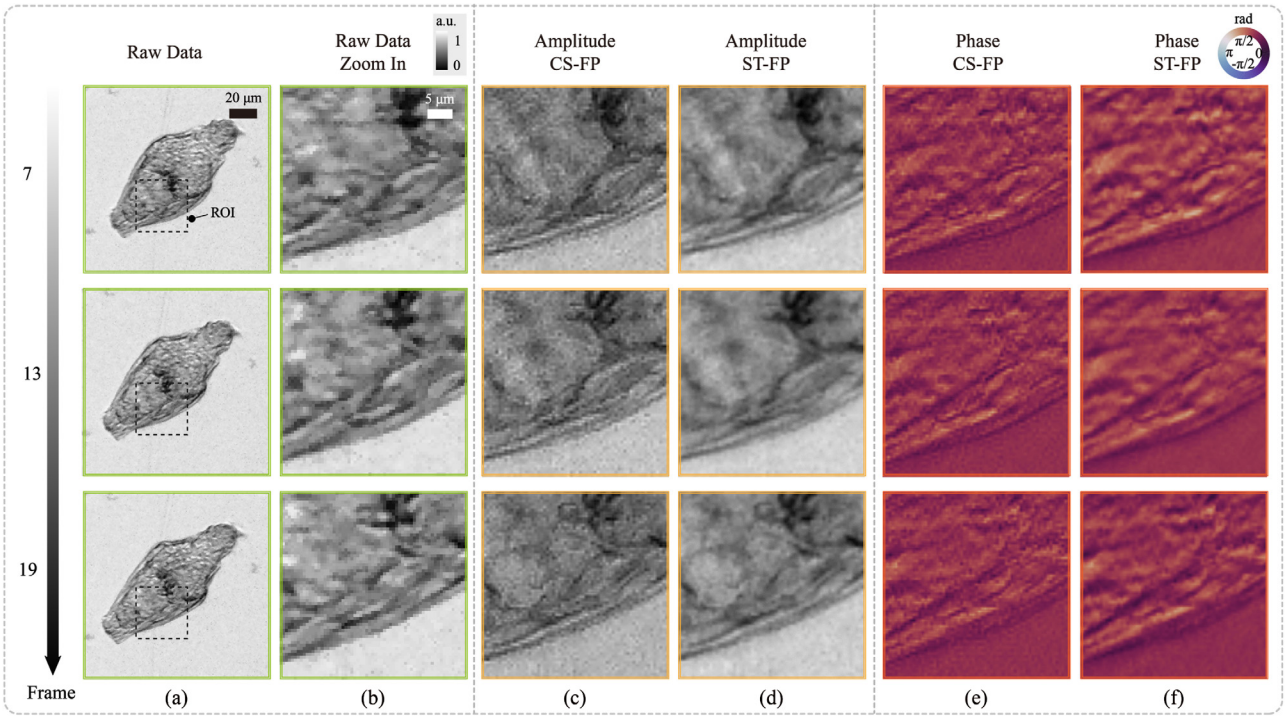

Fig. 5. Results comparison of a live rotifer at different times. (a) LR raw data. (b) ROI from (a). (c), (d) Amplitude results of CS-FP and our method. (e), (f) Phase results of CS-FP and our method.

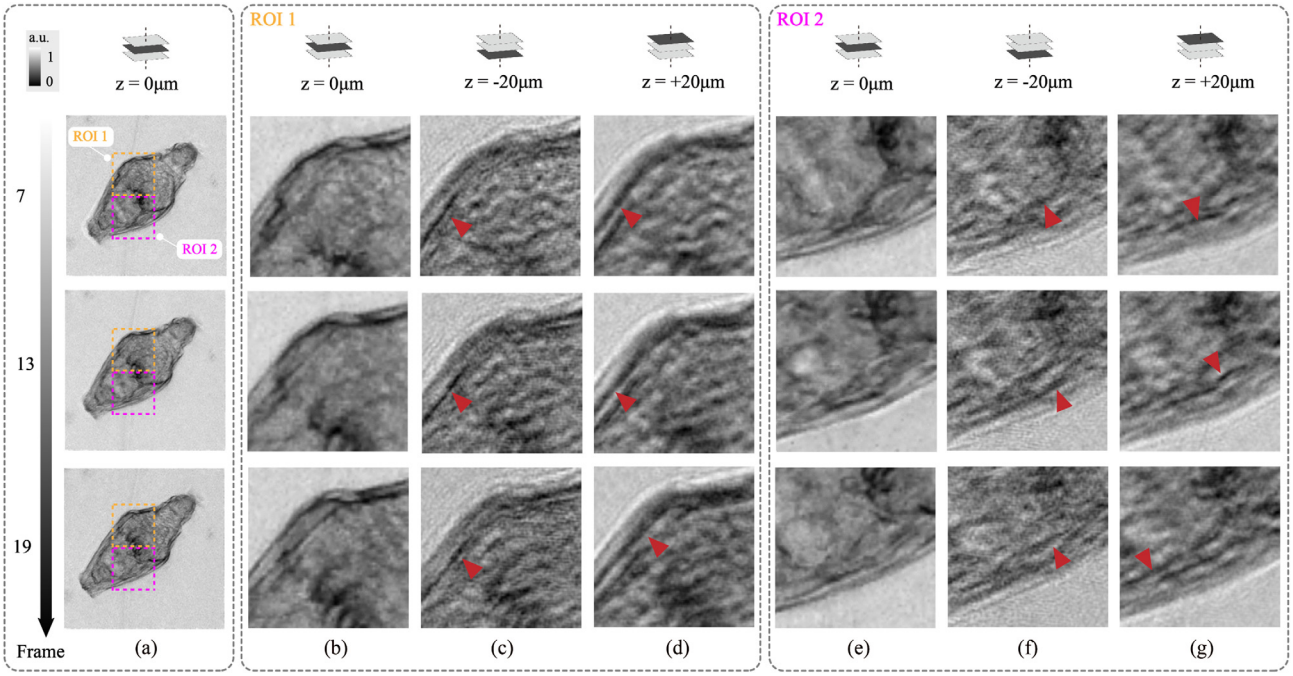

Fig. 6. Temporal digital refocusing on a rotifer dataset across various propagation distances. (a) Reconstruction results of our method in zero plane across different frame times with ROI 1 and ROI 2. (b)–(d) The amplitude profiles of ROI 1 at some specific frames, showcasing the refocusing effects at distances of 0 μm (the reference plane), −20 μm, and 20 μm, respectively. (e)–(g) The refocusing results for ROI 2. Red arrows highlight areas where edge clarity and definition are significantly improved.

if the motion is fast enough to cause motion blur within a single exposure, our method cannot recover sharp features. To address this limitation, future work could focus on training neural networks with known motion blur characteristics, to develop models that can deblur images or accurately predict the underlying sharp features.

In regard to the applications, ST-FP could revolutionize the study of dynamics like droplet generation [76] and other fluid mechanics applications [77–79]. It could also catalyze extensive research into novel medium combination processes across various industries [80]. Significantly, our findings underscore the value of tardigrades as a comparative system to understand the mechanics underlying coordination in panarthropod locomotion. Moreover, tardigrades serve as a vital reference for the design and control of small, soft-bodied locomotive systems, spanning from natural organisms to robotics [81]. ST-FP stands as a pivotal tool in both scientific exploration and technological innovation.

In conclusion, we propose a highly innovative approach, space-time Fourier ptychography (ST-FP), for reconstructing dynamic microscopic scenes by aligning spatial and temporal information. This approach combines optical flow estimation with fast FP imaging methodology, utilizing random multiplexing patterns within a customized optimization framework. We demonstrate that the proposed method achieves a symbiotic improvement in accuracy by correlating fluid velocity fields with the recovered complex-valued objects across different timeframes. Furthermore, ST-FP reduces extensive hardware setup, enabling its successful application across various practical scenarios, including live tardigrades, mixed-type rotifers, and moving targets. ST-FP has shown robust capabilities in reconstructing substantial portions of the internal structures of specimens with high accuracy, particularly after employing a digital refocusing technique.

Funding. King Abdullah University of Science and Technology (Individual Baseline Research Fund).

Acknowledgment. The authors thank Dr. Qiang Fu and Dr. Hadi Amata from the Visual Computing Center at King Abdullah University of Science and Technology for constructive discussions and sample fabrication support.

Disclosures. The authors declare no conflicts of interest.

Data availability. Data underlying the results presented in this paper are not publicly available at this time but may be obtained from the authors upon reasonable request.

Supplemental document. See Supplement 1 for supporting content.

REFERENCES

1. A. P. Cuny, F. P. Schlottmann, J. C. Ewald, *et al.*, "Live cell microscopy: from image to insight," Biophys. Rev. **3**, 021302 (2022).
2. R. Ananthakrishnan and A. Ehrlicher, "The forces behind cell movement," Int. J. Biol. Sci. **3**, 303–317 (2007).
3. R. Eils and C. Athale, "Computational imaging in cell biology," J. Cell Biol. **161**, 477–481 (2003).
4. A. G. Godin, B. Lounis, and L. Cognet, "Super-resolution microscopy approaches for live cell imaging," Biophys. J. **107**, 1777–1784 (2014).
5. A. G. York, S. H. Parekh, D. D. Nogare, *et al.*, "Resolution doubling in live, multicellular organisms via multifocal structured illumination microscopy," Nat. Methods **9**, 749–754 (2012).
6. L. Shao, P. Kner, E. H. Rego, *et al.*, "Super-resolution 3D microscopy of live whole cells using structured illumination," Nat. Methods **8**, 1044–1046 (2011).
7. P. Stachelek, L. MacKenzie, D. Parker, *et al.*, "Circularly polarised luminescence laser scanning confocal microscopy to study live cell chiral molecular interactions," Nat. Commun. **13**, 553 (2022).
8. G. Wang, K.-Y. Pu, X. Zhang, *et al.*, "Star-shaped glycosylated conjugated oligomer for two-photon fluorescence imaging of live cells," Chem. Mater. **23**, 4428–4434 (2011).
9. V. Westphal, S. O. Rizzoli, M. A. Lauterbach, *et al.*, "Video-rate far-field optical nanoscopy dissects synaptic vesicle movement," Science **320**, 246–249 (2008).

10. J. Tønnesen, G. Katona, B. Rózsa, *et al.*, "Spine neck plasticity regulates compartmentalization of synapses," Nat. Neurosci. **17**, 678–685 (2014).
11. A. Descloux, K. Grußmayer, E. Bostan, *et al.*, "Combined multi-plane phase retrieval and super-resolution optical fluctuation imaging for 4D cell microscopy," Nat. Photonics **12**, 165–172 (2018).
12. W. Wang, D. Douglas, J. Zhang, *et al.*, "Live-cell imaging and analysis reveal cell phenotypic transition dynamics inherently missing in snapshot data," Sci. Adv. **6**, eaba9319 (2020).
13. G. McConnell, J. Trägärdh, R. Amor, *et al.*, "A novel optical microscope for imaging large embryos and tissue volumes with sub-cellular resolution throughout," eLife **5**, e18659 (2016).
14. S. L. Gupton and C. M. Waterman-Storer, "Spatiotemporal feedback between actomyosin and focal-adhesion systems optimizes rapid cell migration," Cell **125**, 1361–1374 (2006).
15. J. Fan, J. Suo, J. Wu, *et al.*, "Video-rate imaging of biological dynamics at centimetre scale and micrometre resolution," Nat. Photonics **13**, 809–816 (2019).
16. S. Manley, J. M. Gillette, G. H. Patterson, *et al.*, "High-density mapping of single-molecule trajectories with photoactivated localization microscopy," Nat. Methods **5**, 155–157 (2008).
17. B. Ghosh and K. Agarwal, "Viewing life without labels under optical microscopes," Commun. Biol. **6**, 559 (2023).
18. Y. Park, C. Depeursinge, and G. Popescu, "Quantitative phase imaging in biomedicine," Nat. Photonics **12**, 578–589 (2018).
19. T. L. Nguyen, S. Pradeep, R. L. Judson-Torres, *et al.*, "Quantitative phase imaging: recent advances and expanding potential in biomedicine," ACS Nano **16**, 11516–11544 (2022).
20. J. Reed, J. Chun, T. A. Zangle, *et al.*, "Rapid, massively parallel single-cell drug response measurements via live cell interferometry," Biophys. J. **101**, 1025–1031 (2011).
21. P. J. De Groot, "Vibration in phase-shifting interferometry," J. Opt. Soc. Am. A **12**, 354–365 (1995).
22. S. Ri, T. Takimoto, P. Xia, *et al.*, "Accurate phase analysis of interferometric fringes by the spatiotemporal phase-shifting method," J. Opt. **22**, 105703 (2020).
23. P. Marquet, B. Rappaz, P. J. Magistretti, *et al.*, "Digital holographic microscopy: a noninvasive contrast imaging technique allowing quantitative visualization of living cells with subwavelength axial accuracy," Opt. Lett. **30**, 468–470 (2005).
24. H. Lichte and M. Lehmann, "Electron holography-basics and applications," Rep. Prog. Phys. **71**, 016102 (2007).
25. P. Bon, G. Maucort, B. Wattellier, *et al.*, "Quadriwave lateral shearing interferometry for quantitative phase microscopy of living cells," Opt. Express **17**, 13080–13094 (2009).
26. M. Beleggia, M. Schofield, V. Volkov, *et al.*, "On the transport of intensity technique for phase retrieval," Ultramicroscopy **102**, 37–49 (2004).
27. L. Tian and L. Waller, "Quantitative differential phase contrast imaging in an LED array microscope," Opt. Express **23**, 11394–11403 (2015).
28. M. Chen, Z. F. Phillips, and L. Waller, "Quantitative differential phase contrast (DPC) microscopy with computational aberration correction," Opt. Express **26**, 32888–32899 (2018).
29. G. Zheng, R. Horstmeyer, and C. Yang, "Wide-field, high-resolution Fourier ptychographic microscopy," Nat. Photonics **7**, 739–745 (2013).
30. G. Zheng, C. Shen, S. Jiang, *et al.*, "Concept, implementations and applications of Fourier ptychography," Nat. Rev. Phys. **3**, 207–223 (2021).
31. A. Pan, C. Zuo, and B. Yao, "High-resolution and large field-of-view Fourier ptychographic microscopy and its applications in biomedicine," Rep. Prog. Phys. **83**, 096101 (2020).
32. X. Ou, R. Horstmeyer, C. Yang, *et al.*, "Quantitative phase imaging via Fourier ptychographic microscopy," Opt. Lett. **38**, 4845–4848 (2013).
33. Y. Shu, J. Sun, J. Lyu, *et al.*, "Adaptive optical quantitative phase imaging based on annular illumination Fourier ptychographic microscopy," PhotoniX **3**, 24 (2022).
34. R. Wu, Z. Luo, M. Liu, *et al.*, "Fast Fourier ptychographic quantitative phase microscopy for in vitro label-free imaging," Biomed. Opt. Express **15**, 95–113 (2024).
35. J. Kim, B. M. Henley, C. H. Kim, *et al.*, "Incubator embedded cell culture imaging system (emsight) based on Fourier ptychographic microscopy," Biomed. Opt. Express **7**, 3097–3110 (2016).
36. S. Jiang, P. Song, T. Wang, *et al.*, "Spatial-and Fourier-domain ptychography for high-throughput bio-imaging," Nat. Protoc. **18**, 2051–2083 (2023).
37. T. Aidukas, P. C. Konda, and A. R. Harvey, "High-speed multi-objective Fourier ptychographic microscopy," Opt. Express **30**, 29189–29205 (2022).
38. X. He, C. Liu, and J. Zhu, "Single-shot Fourier ptychography based on diffractive beam splitting," Opt. Lett. **43**, 214–217 (2018).
39. Y. Xiao, S. Wei, S. Xue, *et al.*, "High-speed Fourier ptychographic microscopy for quantitative phase imaging," Opt. Lett. **46**, 4785–4788 (2021).
40. L. Tian, Z. Liu, L.-H. Yeh, *et al.*, "Computational illumination for high-speed in vitro Fourier ptychographic microscopy," Optica **2**, 904–911 (2015).
41. S. Simeonov and T. E. Schäffer, "High-speed scanning ion conductance microscopy for sub-second topography imaging of live cells," Nanoscale **11**, 8579–8587 (2019).
42. J. A. Nirody, L. A. Duran, D. Johnston, *et al.*, "Tardigrades exhibit robust interlimb coordination across walking speeds and terrains," Proc. Natl. Acad. Sci. USA **118**, e2107289118 (2021).
43. X. Yin, W. Jin, Y. Zhou, *et al.*, "Hidden defensive morphology in rotifers: benefits, costs, and fitness consequences," Sci. Rep. **7**, 4488 (2017).
44. A. Hamel, C. Fisch, L. Combettes, *et al.*, "Transitions between three swimming gaits in paramecium escape," Proc. Natl. Acad. Sci. USA **108**, 7290–7295 (2011).
45. S. Lass and P. Spaak, "Chemically induced anti-predator defences in plankton: a review," Hydrobiologia **491**, 221–239 (2003).
46. Y. Gao and L. Cao, "Motion-resolved, reference-free holographic imaging via spatiotemporally regularized inversion," Optica **11**, 32–41 (2024).
47. R. Cao, F. L. Liu, L.-H. Yeh, *et al.*, "Dynamic structured illumination microscopy with a neural space-time model," in *IEEE International Conference on Computational Photography (ICCP)*, IEEE Computer Society, Los Alamitos, California, USA, 2022), pp. 1–12.
48. J. Yoo, K. H. Jin, H. Gupta, *et al.*, "Time-dependent deep image prior for dynamic MRI," IEEE Trans. Med. Imaging **40**, 3337–3348 (2021).
49. P. Bohra, T.-A. Pham, Y. Long, *et al.*, "Dynamic Fourier ptychography with deep spatiotemporal priors," Inverse Probl. **39**, 064005 (2023).
50. C. Mory, V. Auvray, B. Zhang, *et al.*, "Cardiac C-arm computed tomography using a 3D + time roi reconstruction method with spatial and temporal regularization," Med. Phys. **41**, 021903 (2014).
51. J. Wang and X. Gu, "Simultaneous motion estimation and image reconstruction (SMEIR) for 4D cone-beam CT," Med. Phys. **40**, 101912 (2013).
52. G. Zang, R. Idoughi, R. Tao, *et al.*, "Space-time tomography for continuously deforming objects," ACM Trans. Graph. **37**, 100 (2018).
53. G. Zang, R. Idoughi, R. Tao, *et al.*, "Warp-and-project tomography for rapidly deforming objects," ACM Trans. Graph. **38**, 86 (2019).
54. N. Chen, C. Wang, and W. Heidrich, "Snapshot space–time holographic 3D particle tracking velocimetry," Laser Photon. Rev. **15**, 2100008 (2021).
55. X. Li, L. Li, X. Liu, *et al.*, "Dictionary-based compressive Fourier ptychography," Opt. Lett. **47**, 2314–2317 (2022).
56. S. Boyd, N. Parikh, E. Chu, *et al.*, "Distributed optimization and statistical learning via the alternating direction method of multipliers," Found. Trends Mach. Learn. **3**, 1–122 (2011).
57. M. Werlberger, W. Trobin, T. Pock, *et al.*, "Anisotropic Huber-L1 optical flow," in *British Machine Vision Conference* (2009), pp. 1–11.
58. L. Tian, X. Li, K. Ramchandran, *et al.*, "Multiplexed coded illumination for Fourier ptychography with an LED array microscope," Biomed. Opt. Express **5**, 2376–2389 (2014).
59. E. Meinhardt-Llopis and J. Sánchez, "Horn-Schunck optical flow with a multi-scale strategy," Image Process. Line **3**, 151–172 (2013).
60. T. Chu and W. Ranson, "Applications of digital-image-correlation techniques to experimental mechanics," Exp. Mech. **25**, 232–244 (1985).
61. C. A. Glasbey and K. V. Mardia, "A review of image-warping methods," J. Appl. Statist. **25**, 155–171 (1998).
62. J. Sánchez Pérez, E. Meinhardt-Llopis, and G. Facciolo, "TV-L1 optical flow estimation," Image Process. Line **3**, 137–150 (2013).
63. A. Wedel, T. Pock, C. Zach, *et al.*, *An Improved Algorithm for TV-L1 Optical Flow* (Springer, 2009), pp. 23–45.
64. G. Zhou, S. Zhang, Y. Hu, *et al.*, "Adaptive high-dynamic-range Fourier ptychography microscopy data acquisition with a red-green-blue camera," Opt. Lett. **45**, 4956–4959 (2020).
65. M. McPhail, A. Fontaine, M. Krane, *et al.*, "Correcting for color crosstalk and chromatic aberration in multicolor particle shadow velocimetry," Meas. Sci. Technol. **26**, 025302 (2015).
66. L. Bian, G. Zheng, K. Guo, *et al.*, "Motion-corrected Fourier ptychography," Biomed. Opt. Express **7**, 4543–4553 (2016).

67. X. Ou, G. Zheng, and C. Yang, "Embedded pupil function recovery for Fourier ptychographic microscopy," Opt. Express **22**, 4960–4972 (2014).
68. B. Reddy and B. Chatterji, "An FFT-based technique for translation, rotation, and scale-invariant image registration," IEEE Trans. Image Process. **5**, 1266–1271 (1996).
69. H. Zhou, C. Shen, M. Liang, *et al.*, "Analysis of postreconstruction digital refocusing in Fourier ptychographic microscopy," Opt. Eng. **61**, 073102 (2022).
70. S. Zhang, G. Zhou, C. Zheng, *et al.*, "Fast digital refocusing and depth of field extended Fourier ptychography microscopy," Biomed. Opt. Express **12**, 5544–5558 (2021).
71. M. Sun, L. Shao, J. Zhang, *et al.*, "High-resolution 3D Fourier ptychographic reconstruction using a hemispherical illumination source with multiplexed-coded strategy," Biomed. Opt. Express **13**, 2050–2067 (2022).
72. J. Li, A. Matlock, Y. Li, *et al.*, "High-speed in vitro intensity diffraction tomography," Adv. Photon. **1**, 066004 (2019).
73. A. Matlock and L. Tian, "High-throughput, volumetric quantitative phase imaging with multiplexed intensity diffraction tomography," Biomed. Opt. Express **10**, 6432–6448 (2019).
74. J. Li, J. Hao, X. Wang, *et al.*, "Fourier ptychographic microscopic reconstruction method based on residual hybrid attention network," Sensors **23**, 7301 (2023).
75. H. Zhou, B. Y. Feng, H. Guo, *et al.*, "Fourier ptychographic microscopy image stack reconstruction using implicit neural representations," Optica **10**, 1679–1687 (2023).
76. T. Kamal, L. Yang, and W. M. Lee, "In situ retrieval and correction of aberrations in moldless lenses using Fourier ptychography," Opt. Express **26**, 2708–2719 (2018).
77. A. Jahn, F. Lucas, R. A. Wepf, *et al.*, "Freezing continuous-flow self-assembly in a microfluidic device: toward imaging of liposome formation," Langmuir **29**, 1717–1723 (2013).
78. A. Jahn, S. M. Stavis, J. S. Hong, *et al.*, "Microfluidic mixing and the formation of nanoscale lipid vesicles," ACS Nano **4**, 2077–2087 (2010).
79. M. Madadelahi, L. F. Acosta-Soto, S. Hosseini, *et al.*, "Mathematical modeling and computational analysis of centrifugal microfluidic platforms: a review," Lab Chip **20**, 1318–1357 (2020).
80. P. C. Konda, L. Loetgering, K. C. Zhou, *et al.*, "Fourier ptychography: current applications and future promises," Opt. Express **28**, 9603–9630 (2020).
81. T. Li, S. Yu, B. Sun, *et al.*, "Bioinspired claw-engaged and biolubricated swimming microrobots creating active retention in blood vessels," Sci. Adv. **9**, eadg4501 (2023).